

# Precise Single-Frequency Positioning Using Low-Cost Receiver with the Aid of Lane-Level Map Matching for Land Vehicle Navigation

Fei Liu<sup>1</sup>, Yue Liu<sup>2</sup>, Zhixi Nie<sup>3</sup> and Yang Gao<sup>4</sup>

<sup>1</sup>*(Department of Civil Engineering, University of Calgary, Calgary, Alberta, Canada)*

<sup>2</sup>*(College of Automation, Harbin Engineering University, Harbin, Heilongjiang, China)*

<sup>3</sup>*(College of Oceanography and Space Informatics, China University of Petroleum, Qingdao, China)*

<sup>4</sup>*(Department of Geomatics Engineering, University of Calgary, Calgary, Alberta, Canada)*

(E-mail: [liu19@ucalgary.ca](mailto:liu19@ucalgary.ca))

Precise positioning with low-cost single-frequency global navigation satellite system (GNSS) receivers has great potential in a wide range of applications because of its low price and improved accuracy. However, challenges remain in achieving reliable and accurate solutions using low-cost receivers. For instance, the successful ambiguity fixing rate could be low for real-time kinematic (RTK) while large errors may occur in precise point positioning (PPP) in some scenarios (e.g., trees along the road). To solve the problems, this paper proposes a method with the aid of additional lane-level digital map information to improve the accuracy and reliability of RTK and PPP solutions. In the method, a digital camera will be applied for lane recognition and the positioning solution from a low-cost receiver will be projected to the digital map lane link. With the projected point position as a constraint, the RTK ambiguity fixing rate and PPP performance can be enhanced. A field kinematic test was conducted to verify the improvement of the RTK and PPP solutions with the aid of map matching. The results show that the RTK ambiguity fixing rate can be increased and the PPP positioning error can be reduced by map matching.

## KEYWORDS

1. Single Frequency.
2. Low Cost.
3. Map Matching.
4. Precise Point Positioning.
5. Real-Time Kinematic.

Submitted: 17 March 2020. Accepted: 24 June 2020. First published online: 23 July 2020.

1. INTRODUCTION. With the increased measurement quality of single-frequency global navigation satellite system (GNSS) receivers, precise single-frequency positioning is attracting academic and industrial attention. Precise point positioning (PPP) and real-time kinematic (RTK) are two main approaches to achieve high-precision solutions with

single-frequency GNSS receivers. With the availability of precise satellite ephemeris products and ionosphere products, single-frequency PPP (SF-PPP) using low-cost receivers is capable of achieving decimetre-level solutions (de Bakker and Tiberius, 2017; Nie et al., 2019; Nie et al., 2020). Lane-level PPP products are also available in the market (Profound Positioning Inc., 2019). However, it is still inevitable that SF-PPP will suffer occasional large errors (over 1 m) in some scenarios. Unlike PPP, RTK requires a rover station and a base station to apply differential algorithms to remove the common error sources. Numerous studies have investigated single-frequency RTK using low-cost receivers (Odolinski and Teunissen, 2017, 2018). Single-frequency RTK (SF-RTK) can use low-cost receivers to achieve centimetre-level solutions with ambiguities fixed. However, it is still challenging for SF-RTK to fix the ambiguities instantaneously and correctly in dynamic mode.

To overcome the drawbacks in SF-PPP and SF-RTK, the inertial navigation system (INS) is usually integrated with GNSS positioning. Liu et al. 2018 tightly integrated SF-PPP and INS for land vehicle navigation in a challenging environment. Han et al. 2017 and Li et al. 2017 integrated inertial measurements to aid SF-RTK ambiguity resolution (AR), which effectively improves the successful fixing rate. However, the accuracy of the SF-PPP/INS integration is dominated by the SF-PPP. The improvement of SF-RTK AR depends on the accuracy of INS mechanisation, which may be not reliable after a relatively long time of error accumulation.

In addition to inertial sensors, map matching can also provide external position information, which can be integrated with GNSS positioning. Balazadegan Sarvrood et al. 2018 applied map matching for dual-frequency PPP to improve the float solutions. Liu 2017 further adopted the aid of map matching to accelerate the PPP AR. All the above studies are based on a single-lane road where the projection of the GNSS solution on the road link is simple and accurate. However, in practical applications, there are multiple lanes on the road, which makes the map matching more difficult. Limited research has applied the lane-level digital map to aid the single-frequency GNSS positioning. Recently, the precise lane-level digital map has become available and lane-detection technology is maturing, which inspired the authors to investigate the precise single-frequency GNSS positioning with the aid of lane-level map matching. In this research, global positioning system (GPS) observations from a low-cost u-blox receiver are used for RTK and PPP. An industrial camera is applied to take images of the road every second to recognise the lane that the vehicle is moving on. With the recognised lane on the image, the GPS solution can be projected on the specific lane link. With the projected point as measurement constraints, some large errors in SF-PPP can be reduced and the overall positioning accuracy can be improved. For SF-RTK, the ambiguity fixing rate is supposed to be improved due to the external position information, which shrinks the search areas of integer ambiguities.

This paper is organised as follows. The SF-PPP and SF-RTK are briefly introduced in Section 2; the lane recognition and map matching methods used in this research are illustrated in Section 3; Section 4 explains the method to integrate the map matching and GNSS solution. Field tests and results are presented in Section 5. The conclusions are given in Section 6.

**2. FUNDAMENTALS OF SF-PPP AND SF-RTK.** In this section, the fundamentals of SF-PPP and SF-RTK are reviewed in Section 2.1 and Section 2.2 respectively.

2.1. *SF-PPP*. PPP utilises precise satellite products and calibrates the error sources to achieve centimetre-level to decimetre-level positioning accuracy with a single receiver. Since single-frequency low-cost GNSS receivers dominate the market, SF-PPP has been investigated in recent years (de Bakker and Tiberius, 2017; Nie et al., 2019; Nie et al., 2020). The single-frequency PPP positioning model can be given as

$$\begin{aligned} P_1 &= \rho + c \cdot dt_r - c \cdot dt^s + T + I + B_{pr} - B^{ps} + \varepsilon_P \\ L_1 &= \rho + c \cdot dt_r - c \cdot dt^s + T - I + \lambda_1 \cdot N_1 + b_{lr} - b^{ls} + \varepsilon_L \end{aligned} \quad (1)$$

where  $P_1$  and  $L_1$  are the code and carrier-phase measurements of L1 (unit: metre);  $\rho$  is the geometric distance between the satellite and receiver;  $c$  is the light speed;  $dt_r$  represents the receiver clock offset;  $dt^s$  is the satellite clock offset;  $T$  is the tropospheric delay;  $I$  is the ionospheric effect on L1;  $\lambda_1$  and  $N_1$  represent the wavelength and the integer ambiguity;  $B_{pr}$  and  $B^{ps}$  are the receiver and satellite code biases; similarly,  $b_{lr}$  and  $b^{ls}$  are the phase biases at the receiver- and satellite-end;  $\varepsilon_P$  and  $\varepsilon_L$  are the corresponding measurement noise.

In Equation (1), the satellite orbit and clock errors can be corrected with precise satellite products. Since most precise satellite products are referred to dual-frequency ionosphere-free code measurements, the code and phase biases on the right side of Equation (1) should be considered carefully. The satellite code bias can be corrected with the application of C1-P1 and P1-P2 differential code biases (DCB) products. Considering that the receiver code bias cannot be separated from the receiver clock offset, they are estimated as one unknown in the estimator. The phase biases are absorbed into ambiguities in the estimator. The tropospheric delay can be corrected by the Saastamoninen model (Saastamoinen, 1972) while the ionospheric delay can be relieved with the application of ionospheric products (e.g. IGS Global Ionospheric Map, CNES, VTEC, SSR etc.) (Schaer, 1997; Schaer et al., 1998; CNES, 2019). In addition to the errors listed in Equation (1), other error sources (e.g., the Sagnac effect, special relativistic effect, Shapiro time delay, satellite/receiver antenna phase centre offset and phase centre variation, phase wind-up effect etc.) also have to be calibrated before estimation (Wu et al., 1992; Ashby, 2003; Schmid et al., 2007). In other words, only the position and clock errors together with ambiguities are estimated. With the methods applied in this work, the positioning accuracy can reach within a few decimetres with a few seconds of convergence time. Due to the existence of ionosphere residuals, it is difficult to improve the performance without external aids (e.g. map matching).

2.2. *SF-RTK*. RTK applies the double difference between the base and rover observations to remove the common errors. In this work, a short baseline is applied and the atmospheric delays are assumed to be removed after double difference. The short-baseline SF-RTK positioning model between the base ( $a$ ) and rover ( $b$ ) for GNSS satellite  $i$  and  $j$  can be given as (Tian et al., 2015)

$$\begin{aligned} P_{ab}^{ij} &= \rho_{ab}^{ij} + \delta_{ab}^{ij} + \xi_{ab}^{ij} \\ \lambda^i \phi_{ab}^i - \lambda^j \phi_{ab}^j &= \rho_{ab}^{ij} + \lambda^i N_{ab}^i - \lambda^j N_{ab}^j + \gamma_{ab}^{ij} + \varepsilon_{ab}^{ij} \end{aligned} \quad (2)$$

where  $P_{ij}^{ab}$  (unit: metre) and  $\phi_{ij}^{ab}$  (unit: cycle) are the double-difference code and phase measurements;  $\rho_{ij}^{ab}$  is the double-difference geometric distance;  $\phi_i^{ab}$  and  $\phi_j^{ab}$  are the single-difference between-station phase measurements of satellite  $i$  and  $j$  respectively;  $\lambda^i$  and  $\lambda^j$  are the wavelengths of satellite  $i$  and  $j$  respectively;  $N_i^{ab}$  and  $N_j^{ab}$  are the single-difference ambiguities of corresponding satellites;  $\delta_{ij}^{ab}$  and  $\gamma_{ij}^{ab}$  are the inter-frequency biases

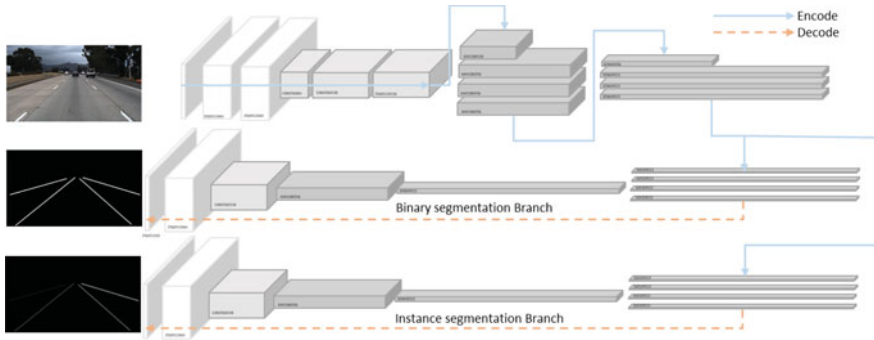


Figure 1. LaneNet architecture. The encoding stage is denoted by blue arrows while the decoding stage is represented by dash orange arrows.

(IFB) in code and phase measurements;  $\xi_{ij}^{ab}$  and  $\varepsilon_{ij}^{ab}$  are the noise of double-difference measurements.

In this paper, GPS measurements are applied. Therefore,  $\delta_{ij}^{ab}$  and  $\gamma_{ij}^{ab}$  are eliminated after double difference. Moreover, the single-difference ambiguities can be added together as double-difference ambiguities due to the same wavelength. After removing all the error sources in RTK, the position unknowns and the double-difference ambiguities are estimated in the estimator. The integer ambiguities in Equation (2) can be fixed and the positioning accuracy can be greatly improved. For dual-frequency RTK (DF-RTK), it is much easier to fix the ambiguities due to redundant measurements. However, it is challenging for SF-RTK to achieve the instantaneous fixed solution in some circumstances especially with low-cost GNSS receivers.

### 3. ROAD LANE DETECTION AND MAP MATCHING.

**3.1. Road lane detection.** Road lane detection and recognition is an important part of the lane departure warning system in a modern automobile including an autonomous car. It also becomes increasingly significant in precise positioning, especially with a precise digital map. The most commonly applied sensor for lane detection is a camera, and the methods based on images can be categorised as mark-feature-based method and machine-learning-based method (Neven et al., 2018; Pan et al., 2018; Zou et al., 2019). Narote et al. 2018 summarised and compared the lane detection methods based on the mark features. Generally, edge detection, colour segment, Hough transform or Kalman filter are applied to detect the lane boundaries. The main drawback of these methods is that they are affected by road scene variations (e.g. lane numbers). Although machine-learning-based methods usually need to train the complicated model with a big dataset, the detection can be more robust and accurate. LaneNet method is applied for lane detection in this paper. The model is trained with TuSimple datasets (TuSimple, 2017). The general procedures are summarised in the following paragraph (Neven et al., 2018; MaybeShewill-CV, 2019).

The convolutional network consists of two branches, namely binary segmentation and instance segmentation, both of which are based on encoder-decoder network Enet (Paszke et al., 2016). The network architecture is shown in Figure 1. The binary segmentation branch is to distinguish the lanes from the background while the instance segmentation branch can distinguish the lanes from each other. The two branches share most of the

encoder stages except for the last one, which makes the last stage in encoder and decoder the backbone of each branch. The loss function for the binary segmentation branch is cross-entropy with bounded inverse class weighting (Paszke et al., 2016) to avoid problems caused by high imbalance between the lanes and backgrounds. For the instance segmentation branch, distance metric learning-based discriminative loss functions are applied to disentangle the lane pixels identified by the segmentation branch (De Brabandere et al., 2017). Clustering is applied to separate the pixel embedding of different road lanes. Specifically, the loss function consists of three terms, namely variance term, distance term and regularisation term, given as

$$\begin{aligned}
 L_{var} &= \frac{1}{C} \sum_{c=1}^C \frac{1}{N_c} \sum_{i=1}^{N_c} [||\mu_c - x_i|| - \delta v]_+^2 \\
 L_{dist} &= \frac{1}{C(C-1)} \sum_{c_A=1}^C \sum_{c_B=1}^C [2\delta d - ||\mu_{c_A} - \mu_{c_B}||]_+^2 \\
 L_{reg} &= \frac{1}{C} \sum_{c=1}^C ||\mu_c|| \\
 L &= L_{var} + L_{dist} + 0.001L_{reg}
 \end{aligned} \tag{3}$$

where  $L$  is the discriminative loss function;  $L_{var}$ ,  $L_{dist}$  and  $L_{reg}$  are the variance term, distance term and regularisation term respectively;  $C$  is the number of clusters in the ground truth;  $N_c$  is the number of elements in cluster  $c$ ;  $x_i$  is the pixel embedding of the lane;  $\mu_c$  is the mean of embedding, namely the centre of the cluster;  $\mu_{c_A}$  and  $\mu_{c_B}$  represent different centres;  $[x]_+ = \max(0, x)$ ;  $\delta v$  and  $\delta d$  are the margins of variance and distance loss.

The variance term imposes an intra-cluster pull force on embedding pixels towards the centre while the distance term pushes the clusters away from each other. The regularisation term is a small pull that keeps the activations bounded. With such a network model, the road lanes can be detected for further applications.

**3.2. Map matching.** Map matching aims to determine the road link on the digital map on which the land vehicle is moving. Based on the land vehicle state (e.g., position, velocity, azimuth etc.) and digital map information, the land vehicle position can be projected on the road link of the digital map. Generally, map matching algorithms can be classified into three categories, namely geometric map matching, topological map matching and advanced map matching (e.g. fuzzy logic map matching). Geometric map matching determines the correct road link based on the relationship between the vehicle localisation and digital map entities. For topological map matching, the topology of the road network is also taken into consideration. Fuzzy logic map matching utilises fuzzy logic to find out the best match of road link, which has been proved to be the one with least mismatching (Quddus, 2006). With an accessible precise digital map, map matching provides external position information in addition to GNSS positioning (Liu, 2017; Balazadegan Sarvrood et al., 2018). In the past, the accuracy of the GNSS solution was low, therefore, it was necessary to adopt more complicated algorithms to avoid mismatching. However, with the development of GNSS positioning technology, the horizontal accuracy could reach lane level (sub-metre) even with low-cost receivers, which enables correct map matching using simply geometric map-matching algorithms. In this research, geometric point-to-point matching is applied. This method finds the closest node of the road network based on the position of the land vehicle, given that the SF-PPP and SF-RTK float solutions can reach decimetre accuracy. Usually, there are multiple lanes within one road, which makes map matching useless without

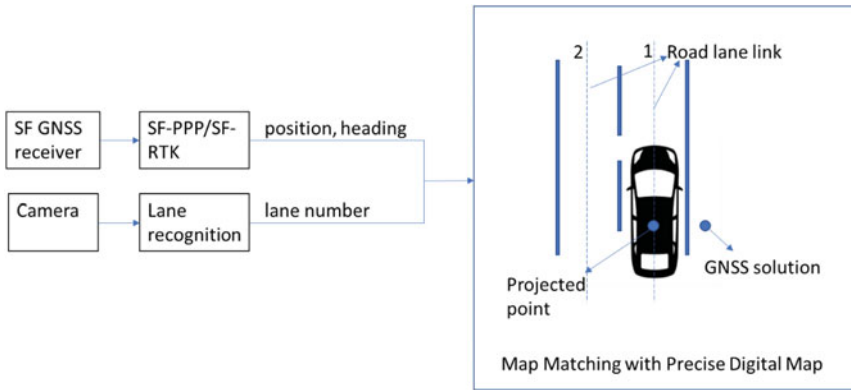


Figure 2. SF-GNSS with aid of lane-level digital map matching.

lane information in precise GNSS positioning. In this paper, the precise lane-level digital map generated based on RTK fixed solution is applied. In addition, the lane detection method introduced before is adopted to find out the lane that the vehicle is moving on. The procedure is summarised in Figure 2.

In Figure 2, GNSS first provides the initial solution, which is projected on the closest road link with two lanes. The digital map used contains the information for both lanes. Therefore, with the detected lane number obtained by lane recognition, the GNSS solution can be projected on the correct lane link.

4. INTEGRATION OF SF-GNSS AND MAP MATCHING. The projected point on the lane link, of which the accuracy can reach a few decimetres on the cross-road direction, can be further applied to reduce the SF-PPP positioning error or used to improve the SF-RTK fixing rate. To be more specific, the two-dimensional (2D) coordinates of the projected points can be applied as additional observations other than the GNSS measurements in the Kalman filter. The processing procedure of the integration is summarised in Figure 3.

In Figure 3, the inputs for map matching are the same as in Figure 2, namely the initial GNSS solution and detected lane number. For map matching, a modified OpenStreetMap (OSM) shapefile is loaded in an open-source relational database management system (RDBMS) named PostgreSQL, which contains several types of the lane link information (e.g. the link ID, link geometry, link type, lane number, link azimuth, start and end node IDs and coordinates in Universal Transverse Mercator etc.). In map matching, the PostgreSQL is connected to manage the spatial queries. One thing that needs to be mentioned is that the accuracy of the original OSM shapefile is in metres, which cannot reach the requirement of this work. Besides, the lane links in each road are unavailable. Therefore, to access lane-level digital maps, the modified shapefile based on RTK fixed solution on each lane is made by QGIS, which is a free geographic information system application that allows creating, editing, visualising and analysing geospatial data. In this shapefile, lane information on several roads is provided. In Figure 3 a feedback filter is designed to exclude those possible mismatched points in map matching, which is important since faulty projected points lead to completely incorrect results. In this work, there are three principles of the feedback filter which are listed as follows. The first one is that if the difference

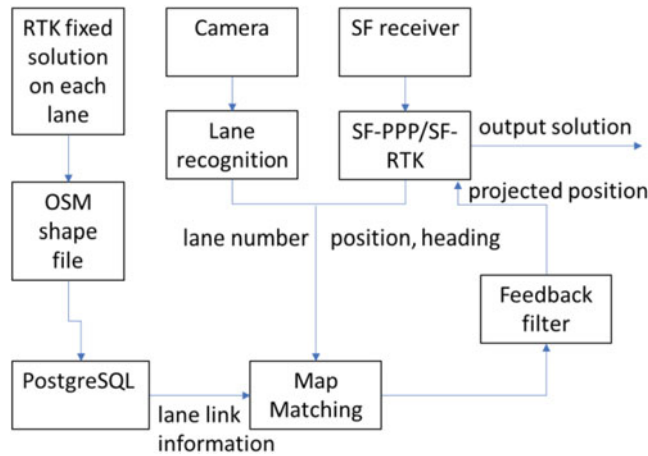


Figure 3. Processing procedures for SF-GNSS with aid of lane-level map matching.

between the heading of the land vehicle and the lane link is larger than a threshold, map matching stops. The second one requires the distance from the land vehicle to a junction less than a threshold (e.g. 5 m) to have valid map matching projected points. The last one stops map matching when lane detection fails.

The additional positioning information from map matching is further applied to improve the SF-GNSS positioning results. Specifically, the Kalman filter is applied to integrate the SF-GNSS and map matching. The projected points on the road lanes from map matching are applied as pseudo measurements in the Kalman filter functioning as constraints of the positioning results. The general Kalman filter calculation procedure is defined in Equation (4) as (Welch and Bishop, 1995)

$$\begin{aligned}
 X_{k+1}^- &= \Phi_{k+1,k} X_k + w_k \\
 P_{k+1}^- &= \Phi_{k+1,k} P_k \Phi_{k+1,k}^T + Q_k \\
 K_{k+1} &= P_{k+1}^- H_{k+1}^T (H_{k+1} P_{k+1}^- H_{k+1}^T + R_{k+1})^{-1} \\
 X_{k+1} &= X_{k+1}^- + K_{k+1} (Z_{k+1} - H_{k+1} X_{k+1}^-) \\
 P_{k+1} &= (I - K_{k+1} H_{k+1}) P_{k+1}^-
 \end{aligned}
 \tag{4}$$

where  $X_{k+1}^-$  is the predicted state vector;  $w_k$  is the process noise vector;  $P_{k+1}^-$  is the covariance of the predicted state vector;  $\Phi_{k+1,k}$  is the transition matrix between two consecutive epochs;  $Q_k$  is the process noise covariance;  $K_{k+1}$  is the optimal gain matrix;  $H_{k+1}$  is the corresponding design matrix;  $R_{k+1}$  is the covariance matrix of the measurements;  $Z_{k+1}$  is the measurement vector;  $I$  is the identity matrix;  $X_{k+1}$  is the updated state vector after applying the measurement;  $P_{k+1}$  is the updated state vector covariance.

In this paper, the position errors, ambiguities and receiver clock offset (for SF-PPP) are estimated as the state vector in the Kalman filter. In addition to the GNSS measurements in Equations (1) and (2) the difference between the GNSS solution and the map matched point is also applied in the measurement update in the Kalman filter. By projecting the GNSS solution on the lane link, the map matching measurement, namely the coordinate difference in the cross-lane direction, can be given as

$$Z_{mm} = \delta c
 \tag{5}$$

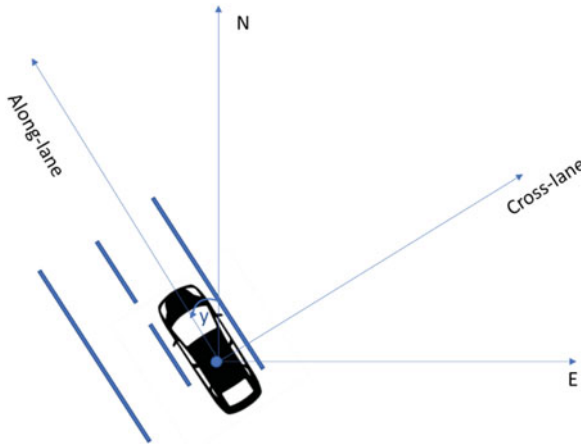


Figure 4. Definition of lane frame.

where  $Z_{mm}$  is the additional measurement formed by map matching, namely the distance between the GNSS solution and the map matched point by projection. The corresponding design matrix can be formed as

$$H_{mm} = [r_{11} \quad r_{12} \quad r_{13} \quad 0 \quad \dots] \tag{6}$$

where  $r_{1i}$  represents the elements for the position corrections in the state vector while the other elements are 0. The  $r_{1i}$  is the first row of the rotation matrix  $R$  from ECEF (Earth-centred, Earth-fixed frame) to the lane frame that is defined as the x-axis pointing to the cross-lane direction, y-axis pointing to the along-lane direction while z-axis completes the right-handed coordinate system. The lane frame is defined by the rotation of the local-level frame with a yaw angle  $y$ , which is shown in Figure 4.

The rotation matrix  $R$  from ECEF to the lane frame can be given as

$$R = R_l^m R_e^l = \begin{bmatrix} r_{11} & r_{12} & r_{13} \\ r_{21} & r_{22} & r_{23} \\ r_{31} & r_{32} & r_{33} \end{bmatrix} \tag{7}$$

where  $R$  is the rotation matrix from ECEF to the lane frame;  $r_{11}, r_{12}$  and  $r_{13}$  are the elements in the design matrix in Equation (6);  $R_l^m$  and  $R_e^l$  are the rotation matrices from ECEF to local-level frame and from local-level frame to the lane frame respectively, given as

$$R_l^m = \begin{bmatrix} \cos y & \sin y & 0 \\ -\sin y & \cos y & 0 \\ 0 & 0 & 1 \end{bmatrix} R_e^l = \begin{bmatrix} -\sin \lambda & \cos \lambda & 0 \\ -\sin \varphi \cos \lambda & -\sin \varphi \sin \lambda & \cos \varphi \\ \cos \varphi \cos \lambda & \cos \varphi \sin \lambda & \sin \varphi \end{bmatrix} \tag{8}$$

where  $y$  is the yaw angle;  $\varphi$  and  $\lambda$  are the latitude and longitude.

5. FIELD TESTS AND RESULTS. To verify the effectiveness of the proposed integration of map matching and SF-GNSS, a field kinematic test was conducted in Calgary. The test setup is shown in Figure 5. A u-blox M8U receiver and a NovAtel receiver were





Figure 5. Kinematic test setup.

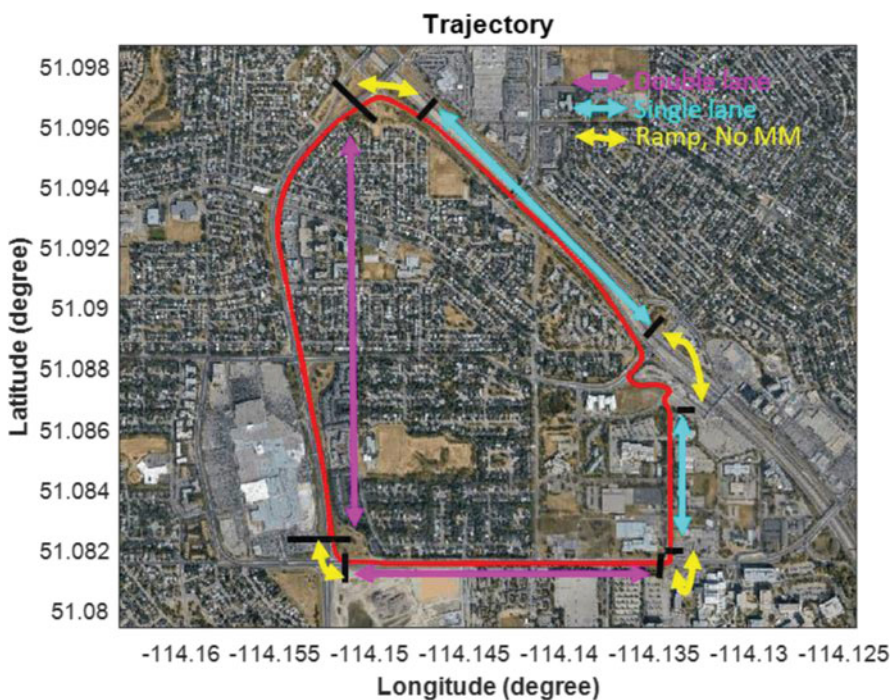


Figure 6. Kinematic test trajectory.

connected to a geodetic antenna on the roof of a land vehicle through a signal splitter. The u-blox receiver is used to conduct the SF-PPP and SF-RTK while the NovAtel receiver is used to conduct dual-frequency RTK with IGS (International GNSS Service) station UCAL as the base. The dual-frequency fixed RTK solution is applied as the reference to evaluate the performance of different methods. For the SF-RTK, the base station is also UCAL. In SF-GNSS processing, GPS code and phase measurements were applied. A PIXELINK camera is used to take images at 1 FPS (frame per second) for lane detection. The u-blox receiver is used to trigger the camera to take images with GPS time tag. All the datasets are



Figure 7. Lane detection.

logged by a laptop and the integration processing is post-mission processed using the collected datasets. The current implementation of SF-GNSS and map matching cannot achieve real-time solutions.

During the test, the land vehicle was moving on 32 Avenue NW, Shaganappi Trail NW, and 33 Street NW. The test environment is suburban, with trees and buildings along the road. For the land vehicle trajectory, 32 Avenue NW and Shaganappi Trail NW are two-lane roads with the more accurate lane information in the digital map while the others are just one-lane roads. When the land vehicle was approaching intersections or ramps, map matching was not applied. The trajectory and lane information are indicated in Figure 6. The roads with two lanes, one lane, and no map matching are marked in magenta, cyan and yellow respectively.

The digital map is made based on the RTK solution with attributes containing the link number, lane order and total number of lanes on the road. When the test was conducted, the digital map was ready. During the test, there were two lanes at most on any road. The right lane and left lane are marked as lane 1 and lane 2 respectively in the digital map. Based on the GPS initial positioning result, the road can be selected on the digital map. With the lane detection result from the images taken by the camera, the lane order can be determined and the GPS positioning result can be projected on the lane link. Figure 7 shows lane detection based on the image taken by the camera. The lane in the left image is detected and marked as white pixels in the right binary image. Based on the location of the detected lane in the image, the moving lane order can be determined.

The satellite number, PDOP (position dilution of precision) and HDOP (horizontal dilution of precision) during the test can be found in Figure 8. During the test, more than eight satellites can be observed for most of the time. The drop of satellite number around 370 s is due to signal blockage by a bridge.

With the external position information, based on Equations (4)–(7), SF-RTK ambiguity fixing rate can be further improved and SF-PPP positioning accuracy can be slightly enhanced with the removal of large errors. Figure 9 shows the SF-RTK positioning results in each direction. The ambiguity ratio in this test is set as 3. In Figure 9, the periods with different numbers of lanes are marked in different colours as in Figure 6. The red, green and blue lines represent positioning errors in east, north and up directions, respectively. State 1 means ambiguities are fixed while state 2 represents unsuccessful ambiguity resolution. The epoch-wise ambiguity fixing method is applied here in which the ambiguities and position are reinitialised every epoch. In this way, if the ambiguities are not fixed, the performance is similar to DGNSS since the Kalman filter is reinitialised. It can be seen that the ambiguity fixing rate is improved, especially during the period with double lanes where the digital map is more accurate. The number of epochs with ambiguities fixed was

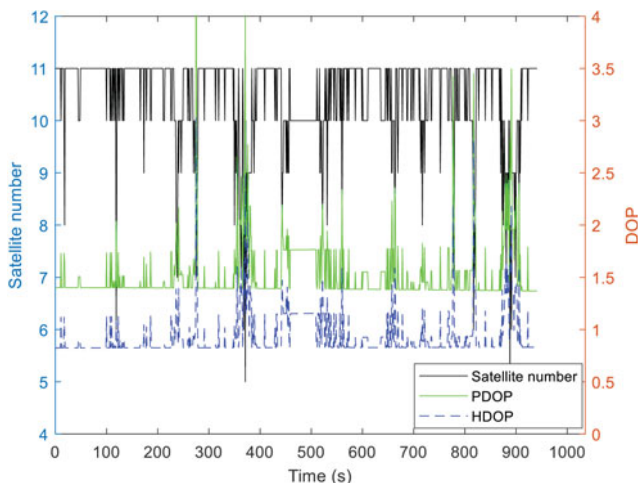


Figure 8. Satellite number and DOP(dilution of precision) values during the test.

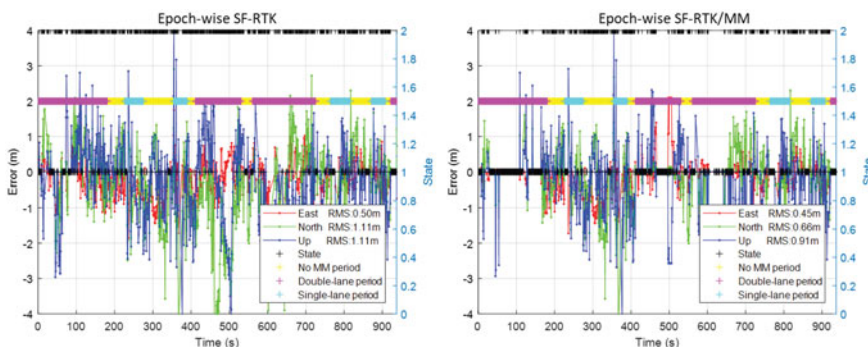


Figure 9. Positioning errors of epoch-wise SF-RTK and SF-RTK/MM.

improved from 252 to 491. With the total number of epochs as 936, the ambiguity fixing rate increased from 26.9% to 52.5%. Due to the improved ambiguity fixing rate, the overall performance of SF-RTK is improved as well. The positioning errors in the horizontal plane and vertical direction were reduced from 1.21 m to 0.80 m and from 1.11 m to 0.91 m respectively.

For the 463 epochs when the land vehicle was moving on the road with two lanes, the number of epochs with successful ambiguity resolution increased from 122 to 333 with the aid of map matching. The improvement during these periods is more obvious, compared with single-lane periods, because of higher digital map accuracy. For the 140 epochs of single-lane periods, the number of fixed solutions was improved from 35 to 58. The improvement for the single-lane period is not as good as the double-lane period because of degraded digital map accuracy.

SF-PPP using the u-blox receiver is also processed with the aid of map matching. The processing strategy of PPP is summarised as follows. Precise products of satellite orbit and clock are applied to correct the satellite-end errors. Since the precise products are referred

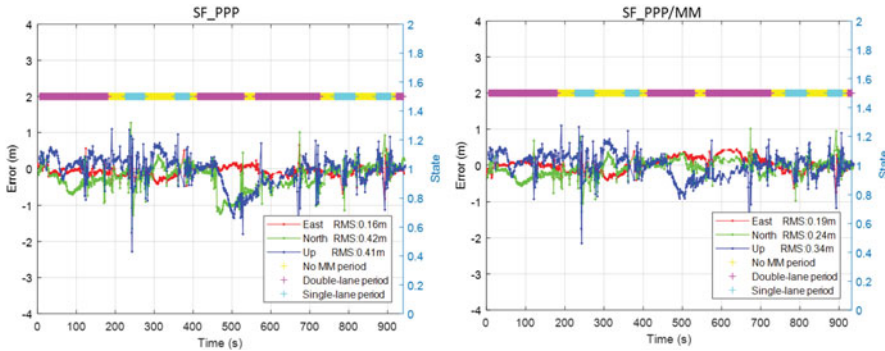


Figure 10. Positioning errors of SF-PPP and SF-PPP/MM.

to ionospheric-free (P1, P2) code, C1-P1 and P1-P2 DCB products are needed to correct the group delay for C1 code measurements of the u-blox receiver. Ionospheric delay is corrected by CODE ionospheric global map while the tropospheric delay is corrected using the Saastamoninen model. The position unknowns and receiver clocks are estimated in the Kalman filter. The residuals of ionospheric delays and tropospheric delays are not included in estimation to simplify the estimation model and reduce the convergence time in practical application. With such a strategy, we can achieve fast solutions with an accuracy of about half a metre. The PPP positioning error plot is shown in Figure 10.

It can be seen that the horizontal accuracy of SF-PPP is improved from 0.45 m to 0.31 m with the aid of map matching. Some large horizontal positioning errors between 450 s and 550 s are reduced with the aid of map matching. Generally, during the 463 epochs of double-lane periods, the horizontal positioning RMS was reduced from 0.52 m to 0.30 m. The improvement in height is less, compared with the horizontal plane, since the 2D digital map is applied without height information. The error in the up direction is reduced from 0.41 m to 0.34 m due to the correlation of position unknowns in different directions.

**6. CONCLUSION.** This paper proposes a method to deploy external precise digital map information to improve the SF-GNSS positioning results. With the aid of map matching, the SF-RTK ambiguity fixing rate and the SF-PPP positioning performance can be improved. A field test was conducted to verify the effectiveness with the aid of map matching. GPS observations from a low-cost u-blox receiver were applied to conduct the single-frequency RTK and PPP. The ambiguity fixing rate of SF-RTK was improved from 26.9% to 52.5%. The overall horizontal positioning error of PPP was reduced from 0.45 m to 0.31 m while the vertical positioning error was reduced from 0.41 m to 0.34 m. During the test, the number of lanes varied on different roads. In this work, the accuracy of the roads with two lanes is the best in the digital map. During the double-lane periods, the improvement for single-frequency positioning is more obvious. Since the 2D digital map was applied, the improvement in height direction for SF-GNSS positioning is limited. Therefore, improvement in PPP height is only about 4 cm.

## ACKNOWLEDGEMENTS

This research is supported by Mitacs Elevate (Ref. IT11518) and the Fundamental Research Funds for the Central Universities (Grant No. 20CX06044A).

## REFERENCES

- Ashby, N. (2003). Relativity in the global positioning system. *Living Reviews in Relativity*, **6**(1), 1.
- Balazadegan Sarvrood, Y., Liu, F. and Gao, Y. (2018). Tight integration of kinematic precise point positioning and digital map for land vehicle localisation. *Survey Review*, **50**(362), 416–424.
- CNES. (2019). The PPP-WIZARD project. Available at: <http://www.ppp-wizard.net/ssr.html>.
- de Bakker, P. F. and Tiberius, C. C. J. M. (2017). Real-time multi-GNSS single-frequency precise point positioning. *GPS Solutions*, **21**(4), 1791–1803.
- De Brabandere, B., Neven, D. and Van Gool, L. (2017). Semantic instance segmentation with a discriminative loss function. *arXiv preprint arXiv:1708.02551*.
- Han, H., et al. (2017). Reliable partial ambiguity resolution for single-frequency GPS/BDS and INS integration. *GPS Solutions*, **21**(1), 251–264.
- Li, T., Zhang, H., Niu, X. and Gao, Z. (2017). Tightly-coupled integration of multi-GNSS single-frequency RTK and MEMS-IMU for enhanced positioning performance. *Sensors*, **17**(11), 2462.
- Liu, F. (2017). Kinematic PPP Ambiguity Resolution with Aid of Map Matching. In *Proceedings of the 30th International Technical Meeting of the Satellite Division of the Institute of Navigation (ION GNSS+ 2017)*. Portland, OR, pp. 4176–4183.
- Liu, Y., Liu, F., Gao, Y. and Zhao, L. (2018). Implementation and analysis of tightly coupled global navigation satellite system precise point positioning/inertial navigation system (GNSS PPP/INS) with insufficient satellites for land vehicle navigation. *Sensors*, **18**(12), 4305.
- MaybeShewill-CV. (2019) LaneNet-Lane-Detection, Github. Available at: <https://github.com/MaybeShewill-CV/lanenet-lane-detection>.
- Narote, S.P., Bhujbal, P.N., Narote, A.S. and Dhane, D.M. (2018). A review of recent advances in lane detection and departure warning system. *Pattern Recognition*, **73**, 216–234.
- Neven, D., et al. (2018). Towards End-to-End Lane Detection: An Instance Segmentation Approach. In *2018 IEEE Intelligent Vehicles Symposium (IV)*. IEEE, pp. 286–291, Changshu, China.
- Nie, Z., Zhou, P., Liu, F., Wang, Z. and Gao, Y. (2019). Evaluation of orbit, clock and ionospheric corrections from five currently available SBAS L1 services: methodology and analysis. *Remote Sensing*, **11**(4), 411.
- Nie, Z., Liu, F. and Gao, Y. (2020). Real-time precise point positioning with a low-cost dual-frequency GNSS device. *GPS Solutions*, **24**(1), 9.
- Odolinski, R. and Teunissen, P. J. G. (2017). Low-cost, high-precision, single-frequency GPS–BDS RTK positioning. *GPS Solutions*, **21**(3), 1315–1330.
- Odolinski, R. and Teunissen, P. J. G. (2018). An assessment of smartphone and low-cost multi-GNSS single-frequency RTK positioning for low, medium and high ionospheric disturbance periods. *Journal of Geodesy*, **93**(5), 701–722.
- Pan, X., Shi, J., Luo, P., Wang, X. and Tang, X. (2018). Spatial as Deep: Spatial CNN for Traffic Scene Understanding. In *Thirty-Second AAAI Conference on Artificial Intelligence*, New Orleans, Louisiana.
- Paszke, A., Chaurasia, A., Kim, S. and Culurciello, E. (2016). Enet: A deep neural network architecture for real-time semantic segmentation. *arXiv preprint arXiv:1606.02147*.
- Profound Positioning Inc. (2019). Profound-IP3. Available at: <http://www.profoundpositioning.com/>.
- Quddus, M. (2006). *High Integrity Map Matching Algorithms for Advanced Transport Telematics Applications*. Centre for Transport Studies, Department of Civil and Environmental Engineering, Imperial College, London UK. Citeseer, p. 270.
- Saastamoinen, J. (1972). Atmospheric correction for the troposphere and stratosphere in radio ranging satellites. In Henriksen, S., Mancini, A. and Chovitz, B. (eds) *The Use of Artificial Satellites for Geodesy*. Washington DC, American Geophysical Union, 15, pp. 247–251.
- Schaer, S. (1997). *How to Use CODE's Global Ionosphere Maps*. Hochschulstrasse, Switzerland, Astronomical Institute, University of Berne, pp. 1–9.
- Schaer, S., Gurtner, W. and Feltens, J. (1998). IONEX: The Ionosphere Map Exchange Format Version 1. In *Proceedings of the IGS AC Workshop*, Darmstadt, Germany.

- Schmid, R., Steigenberger, P., Gendt, G., Ge, M. and Rothacher, M. (2007). Generation of a consistent absolute phase-center correction model for GPS receiver and satellite antennas. *Journal of Geodesy*, **81**(12), 781–798.
- Tian, Y., Ge, M. and Neitzel, F. (2015). Particle filter-based estimation of inter-frequency phase bias for real-time GLONASS integer ambiguity resolution. *Journal of Geodesy*, **89**(11), 1145–1158.
- TuSimple. (2017). tusimple-benchmark, GitHub. Available at: <https://github.com/TuSimple/tusimple-benchmark/wiki>.
- Welch, G. and Bishop, G. (1995). *An Introduction to the Kalman Filter*. Technical Report, Department of Computer Science, University of North Carolina at Chapel Hill.
- Wu, J.T., Wu, S.C., Hajj, G.A., Bertiger, W.I. and Lichten, S.M. (1993). Effects of antenna orientation on GPS carrier phase. *Manuscripta Geodaetica*, **18**(2), 91–98.
- Zou, Q., Jiang, H., Dai, Q., Yue, Y., Chen, L. and Wang, Q. (2019). Robust lane detection from continuous driving scenes using deep neural networks. *arXiv preprint arXiv:1903.02193*.